Response of sub-ice platelet layer thickening rate to variations in Ice Shelf Water supercooling in McMurdo Sound, Antarctica

Chen Cheng[1,2,3], Adrian Jenkins[2], Paul R. Holland[2], Zhaomin Wang[4], Chengyan Liu[4,1,3], and Ruibin Xia[1,3]

[1]Polar Climate System and Global Change Laboratory, Nanjing University of Information Science & Technology, Nanjing, 210044, China
[2]British Antarctic Survey, Cambridge, CB3 0ET, UK
[3]School of Marine Sciences, Nanjing University of Information Science & Technology, Nanjing, 210044, China
[4]College of Oceanography, Hohai University, Nanjing, 210098, China

Correspondence to: Zhaomin Wang (zhaomin.wang@hhu.edu.cn)

Abstract. Persistent outflow of supercooled Ice Shelf Water (ISW) from beneath McMurdo Ice Shelf creates a sub-ice platelet layer (SIPL) having a unique crystallographic structure under the sea ice in McMurdo Sound (MMS), Antarctica. A new frazil-ice-laden ISW plume model that encapsulates the combined nonlinear effects of the vertical distributions of supercooling and frazil ice concentration (FIC) on frazil ice growth is applied to MMS, and is shown to reproduce the observed ISW supercooling and SIPL distributions. Using this model, the dependence of SIPL thickening rate on ISW supercooling in MMS is investigated. Results are found to be sensitive to the choice of frazil ice suspension index, which determines the vertical distribution of FIC. For each suspension index, SIPL thickening rate can be expressed as an exponential function of ISW supercooling. The complex dependence on FIC highlights the need to improve frazil ice observations within the ice-ocean boundary layer.

1 Introduction

Ice shelf basal melting removes more mass from the Antarctic Ice Sheet than iceberg calving does, but the three largest ice shelves, Filchner-Ronne, Ross, and Amery, contribute only 18% of net meltwater flux (Rignot et al., 2013). That is because the seawater-filled cavities beneath those ice shelves are dominated by High Salinity Shelf Water that has a potential temperature at or near the surface freezing point. Ice shelf basal melting occurs at depth, because the freezing point temperature is lower under the elevated pressure, and results in the formation of Ice Shelf Water (ISW), characterized by temperatures below the surface freezing point. When the buoyant ISW ascends along the ice shelf base, the pressure relief causes it to become supercooled in situ, a necessary condition for ice crystals to form and persist in suspension. Those platelet-like frazil ice crystals accumulate under the ice shelves, leading to the formation of marine ice that is thicker and more localized than would be possible through direct freezing at the ice shelf base (Morgan, 1972; Oerter et al. 1992; Fricker et al., 2001; Holland et al., 2007, 2009). Occasionally, frazil ice crystals bathed in supercooled ISW are also carried out beyond the ice shelf front and precipitated under adjacent sea ice, forming an unconsolidated, porous, sub-ice platelet layer

(SIPL) (Hunkeler et al., 2016; Langhorne et al., 2015; Leonard et al., 2006; Robinson et al., 2014). The SIPL not only harbours some of the highest concentrations of sea ice algae on Earth (Arrigo et al., 2010) but also contributes to the sea ice thickness when the water within the pores of the SIPL freezes to become incorporated platelet ice (Smith et al, 2001). In addition, the presence of the SIPL can also exert an influence on the estimation of sea ice thickness from freeboard
5 information obtained by satellite altimetry (Price et al., 2014). Thus, the SIPL should not be ignored when investigating sea ice thickness near an ice shelf front using either numerical models or remote sensing of surface elevation.

Owing to the paucity of direct observation, our understanding of the evolution of frazil-ice-laden ISW is heavily reliant on numerical models mostly derived from plume theory (Holland and Feltham, 2006; Jenkins and Bombosch, 1995; Rees Jones
10 and Wells, 2018; Smedsrud and Jenkins, 2004), which have been widely applied to assess the marine ice beneath the Filchner-Ronne (Bombosch and Jenkins, 1995; Holland et al., 2007; Smedsrud and Jenkins, 2004) and Larsen ice shelves (Holland et al., 2009) and under the sea ice in McMurdo Sound (MMS) (Hughes et al., 2014, hereinafter HU14). To date, all the ISW plume models have been depth-integrated, and all the quantities in these models are treated as vertically-uniform. Recently, Cheng et al. (2017) showed that such an approach, in which supercooling and the resulting frazil ice growth are
15 calculated using a depth-averaged in situ freezing point and vertically-uniform frazil ice concentration (FIC), results in substantial underestimation of marine ice production. Consequently, earlier assessments of marine ice production in the aforementioned areas, such as in MMS, may need to be reevaluated.

MMS, located in the southwestern Ross Sea (Fig. 1), is characterized by significant ISW outflow (HU14; Langhorne et al.,
20 2015; Robinson et al. 2014) and thus a prominent SIPL in the central-western sound (Dempsey et al., 2010); the maximum (area-averaged) observational first-year sea ice and SIPL thickness are 2.5 (2) and 8 (3) m as determined from ice cores recovered adjacent to McMurdo Ice Shelf front between late November and early December in 2011 (Fig. 9 in HU14). The thin (~20 m) McMurdo Ice Shelf front allows the ISW outflow to be delivered to the ocean surface without mixing with warmer ambient waters (Robinson et al., 2014). The study documented in HU14 was the first to apply the steady, one-
25 dimensional frazil-ice-laden ISW plume model developed by Smedsrud and Jenkins (2004), although a constant ISW plume thickness was used. MMS therefore seems an ideal setting in which to apply and evaluate the new vertically-modified ISW plume model proposed by Cheng et al. (2017), which includes time dependence and two horizontal dimensions. The main objective is to quantify for the first time the response of the SIPL thickening rate to variations in ISW supercooling. Establishing such a relationship is of significance to the assessment of total sea ice thickness, and thus the oceanic heat flux
30 associated with the SIPL, in MMS and elsewhere.

Here we first analyze the combined nonlinear effects of the vertical distributions of supercooling and FIC on the suspended frazil ice growth rate in a supercooled ISW plume, and compare results with those obtained with commonly-used, depth-averaged formulation. Then, we evaluate the performance of the vertically-modified ISW plume model in reproducing the

observed ISW supercooling and SIPL distribution to show the necessity of considering the combined nonlinear effects. Finally, we conduct 211 sensitivity simulations with the purpose of quantitatively establishing the response of the SIPL thickening rate to variations in ISW supercooling in MMS.

2 Physically-based formulation for frazil ice growth rate

5   The growth rate of suspended frazil ice, the concentration of which controls both the dynamic and thermodynamic evolution of ISW outflows and the marine ice production rate beneath ice shelves, can be quantified through the following integral expression (Jenkins and Bombosch, 1995),

$$I_{gr} = \int_0^1 T_{SC}\, c_i(\sigma)d\sigma, \quad T_{SC} = T_f(\sigma, S) - T, \tag{1}$$

where $\sigma \in [0,1]$ is the relative vertical coordinate, 0 and 1 respectively correspond to the upper ice-plume and lower plume-
10   ambient water interfaces, T and S are respectively the plume's temperature and salinity, vertically well-mixed within the plume, c_i is the vertically-distributed, in this study, volumetric FIC within the plume, T_{SC} and T_f are respectively the supercooling level (positive for supercooling) and local freezing point. Because of the well-known linear decrease in T_f with increasing water depth, T_{SC} also varies linearly with depth, transitioning from supercooling to overheating as σ increases (Figs. 2a and 3). The corresponding transition height at which $T_{SC} = 0$ is defined by supercooled thickness $D_{SC} = \sigma_{SC}D$
15   where σ_{SC} and D are respectively supercooled fraction and total ISW plume thickness.

In earlier ISW plume models both T_{SC} and c_i are treated as vertically-uniform, being represented by their depth-averaged values $T_{SC}^{0.5}$ (0.5 means at mid-depth) and C_i. Thus, we refer to these ISW plume models as non-vertically-modified (NVM). In reality, however, much like suspended sediment (Cheng et al., 2013, 2016), the FIC should be vertically non-uniform,
20   with higher concentrations near the ice shelf base. A simple expression for the equilibrium vertical profile of FIC can be derived from the one-dimensional advection-diffusion equation, considering only the balance between the buoyant-rise-induced vertical advection and turbulent diffusion terms. The result is an exponential vertical profile of the form (Cheng et al., 2017)

$$\frac{c_i(\sigma)}{C_i} = \frac{6Z_* exp(-6Z_*\sigma)}{1 - exp(-6Z_*\sigma)}, \tag{2}$$

25   where $Z_* = w_i/\kappa u_*$ is the suspension index, w_i is the frazil ice rising velocity, determined by ice crystal size, $u_* = \sqrt{C_d}U$ is the shear velocity related to the turbulent intensity within the ISW plume, C_d the basal drag coefficient, $U = \sqrt{(U_p + U_a)^2 + (V_p + V_a)^2 + U_t^2}$ is the total flow speed, $U_p(U_a)$ and $V_p(V_a)$ are the depth-averaged ISW plume (background current) speed in the x and y directions respectively, U_t is the root-mean square tidal speed, $\kappa = 0.4$ is the von Karman constant. As shown in Fig. 2a, the vertical distribution of FIC is strongly controlled by Z_*. The gradient of the vertical

distribution becomes greater with increasing Z_*, and a vertically-uniform FIC distribution can only be achieved as Z_* approaches 0. Accordingly, Cheng et al. (2017) introduced (2) as well as the linear depth-dependence of supercooling into (1), and as a result significantly improved the simulated pattern of marine ice growth under the western side of Ronne Ice Shelf, compared with the NVM and satellite-derived (Joughin and Padman, 2003) results. Hereinafter, we refer to this

5   vertically-modified ISW plume model as VM.

The dependence of the integral value of I_{gr} on Z_* under specified conditions of supercooling (Fig. 2a) is shown in Fig. 2b, where $D_{SC} = 50$ m in all the cases. It can be seen that the integral value increases nonlinearly with Z_*. The critical Z_* that represents the transition from frazil ice melting ($I_{gr} < 0$) to freezing ($I_{gr} > 0$) decreases as the supercooled part of ISW

10   plume increases. In contrast, owing to the neglect of vertical variation in c_i, the integral values calculated by NVM are constant, leading to transitions from overestimation of frazil ice growth to underestimation, compared with VM, as Z_* increases. Only if the ISW plume is fully supercooled ($\sigma_{SC} = 1$) and Z_* is close to 0 are the integral values of I_{gr} calculated by NVM and VM equal (star in Fig. 2b). These features are illustrated in Fig. 2a: for given supercooling, in order to avoid frazil melting in the lower, overheated part of the ISW plume, Z_* must be large enough to maintain greater FIC in the upper,

15   supercooled part. Owing to the assumption that thermohaline exchanges between frazil crystals and ambient water occur at the crystal edge only for freezing, but over the whole crystal surface for melting (Holland and Feltham, 2006), the integral values of I_{gr} for the lower overheated part can be of much greater magnitude (Fig. 2b). It is therefore necessary to limit the mass loss due to frazil melting in one model time step such that it does not exceed the FIC in the lower, overheated part of the plume. Overall, the FIC and frazil growth rate distributions in the VM model show physically-reasonable and desirable

20   characteristics that are absent from NVM model, and the impacts will be demonstrated by evaluation of the VM model in MMS.

3 ISW model in MMS

The VM and NVM models used in this study are described in detail by Cheng et al. (2017). The governing equations for ISW properties and FIC in both VM and NVM models remain as they were in the depth-integrated, two-dimensional ISW

25   plume model developed by Holland and Feltham (2006), except for the different treatments of the specific terms associated with the frazil ice growth rate, described above, in the FIC and temperature transport equations. Both VM and NVM models combine the same commonly-used parameterizations of thermohaline exchanges across the ice–water interfaces, specifically a three-equation formulation (Holland and Jenkins, 1999) for the sea ice base and a two-equation formulation for frazil ice (Galton-Fenzi et al., 2012), with a multiple size–class frazil dynamics model (Smedsrud and Jenkins, 2004), to calculate

30   basal freezing (f') and frazil melting/freezing (ω'), secondary nucleation (N'), and precipitation (p'). These processes are summarized in Fig. 3. Rather than repeat all the equations here, we recall some of them and present how we set up our ISW plume models on the MMS domain.

The model domain (Fig. 1) is delimited by a 45×40 km² rectangle in the x-y plane with an ISW outflow from beneath McMurdo Ice Shelf. The base of the sea ice in MMS is assumed to be horizontal and rough, owing to the presence of the SIPL. The drag coefficient of the ice underside is therefore 6-30 times larger than that typically applied in ice-ocean

5   interaction models (Robinson et al, 2017). The parameterization of the sea ice thermodynamics, the assumption of no entrainment of ambient water into the ISW plume, and the boundary conditions at the ISW outflow follow HU14. At the outflow the plume thickness is equal to that of the supercooled layer, i.e., $D = D_{SC}$, and the discharge per unit width is 0.02 m² s⁻¹. The addition of both a background circulation and tides follow HU14: the former is assumed to be parallel to the Victoria Land coast, in the negative y direction, and to be constant throughout the model domain; the latter is calculated

10   using root-mean square tidal speeds from Padman and Erofeeva (2005). Because ISW plume in MMS persists for at least the 8-9 months of the ice growth season (Robinson et al., 2014), all runs are integrated for 240 days. The model resolution and time step ($\triangle t$) are 1 km and 25 s, respectively. The frazil ice size distribution is represented by 5 crystal size classes, with the ice concentration at the ISW outflow evenly distributed among them.

15   To calculate SIPL thickness D_{SIPL} at the nth time interval, we adopt the assumptions of HU14 that solid ice fraction within the SIPL is 0.25 (Gough et al., 2012) and that the ice crystals double in volume after precipitation:

$$D_{SIPL} = \frac{1}{0.25} \times 2 \times \sum_{k=1}^{n}(p'_k \times \triangle t), \tag{3}$$

where the frazil ice precipitation rate p' follows the parameterization of McCave and Swift (1976):

$$p' = w_i C_i \left(1 - \frac{U^2}{U_c^2}\right) \times He\left(1 - \frac{U^2}{U_c^2}\right), \tag{4}$$

20   where He is the Heaviside function, U_c is a critical velocity, above which precipitation cannot occur, determined by Shields criterion (Jenkins and Bombosch, 1995).

4 Results

4.1 Standard model run

The performance of the NVM and VM models in reproducing the ISW supercooling and SIPL pattern in MMS are evaluated

25   by comparing results with observational data. The observations, including both oceanographic and ice core data (Fig. 1), are taken from HU14. As this study represents the first application of a two-dimensional ISW plume model to the MMS region, some tuning of model parameters, including the ISW outflow properties, SIPL basal drag coefficient, frazil ice crystal size distribution, background current speed, and Shields criterion (Table 1 gives values adopted key parameters), was required to produce the distributions of ISW properties and SIPL shown in Figs. 4a and 6, respectively. Model results are evaluated by

means of skill metrics: Root-Mean-Square Error (RMSE), Correlation Coefficient (CC), and Skill Score (SS), respectively given by

$$RMSE = \left[\frac{\sum(X_{cal}-X_{obs})^2}{M}\right],$$ (5)

$$CC = \frac{\sum(X_{cal}-\overline{X_{cal}})(X_{obs}-\overline{X_{obs}})}{[\sum(X_{cal}-\overline{X_{cal}})^2 \sum(X_{obs}-\overline{X_{obs}})^2]^{1/2}},$$ (6)

5 $$SS = 1 - \frac{\sum(X_{cal}-X_{obs})^2}{\sum(X_{obs}-\overline{X_{obs}})^2},$$ (7)

where X is the variable being evaluated, M is the number of data points, and the overbar here denotes the arithmetic mean. The performance of model is indicated by SS as: >0.65 excellent; 0.65–0.5 very good; 0.5–0.2 good; <0.2 poor (Luo et al., 2017; Ralston et al., 2010; Song and Wang, 2013).

10 It can be seen that at the end of the simulations both VM and NVM models reproduce the observed values of ISW supercooling at the sea ice base (T_{SC}^0) reasonably well at the five oceanographic sites (Fig. 4a). The skill assessments are summarized in Table 2. The SS of T_{SC}^0 calculated using VM and NVM models are 0.56 and 0.58, respectively, both ranking "very good" according to the categories described above. The CC and RMSE are also reasonable. There are only small differences throughout the time series of T_{SC}^0 simulated by the VM and NVM models (Fig. 4) and the final distributions of

15 both total ISW plume thickness and supercooled thickness are also very similar (see Fig. 5a-d). Actually, a comprehensive comparison of T_{SC}^0 calculated by VM and NVM models will be discussed later through extensive sensitivity experiments (Fig. 8).

In contrast, both of the FIC (red lines in Fig. 4b, Fig. 5e and f) and SIPL thickness (green lines in Fig. 4b, Fig. 6b and c) are

20 underestimated by the NVM model, compared with the result of the VM model, throughout the time series. Given the small differences in T_{SC}^0 calculated by VM and NVM models, this result demonstrates that the vertical distribution of FIC within the ISW plume plays a critical role in determining the suspended frazil ice growth (Fig. 2), and thus the FIC and SIPL thickness distributions. The supercooling is utilized more efficiently in the VM model (that will be discussed in detail later), giving a greater depth-averaged FIC than is produced by the commonly-used NVM model. Because the sea ice base is

25 horizontal, there are no changes in the freezing point associated with pressure change, so supercooling is always highest at the ISW outflow (Fig. 5c and d). That results in the greatest FIC (Fig. 5f) and SIPL thickness (Fig. 6b) near the location of the outflow, with large changes from 2.2×10^{-4} to 4×10^{-5} and 15 to 6 m, respectively, in the case of the VM model within 5 km of the outflow. Referring to the SIPL distribution, although such small-scale changes, if present, were not resolved by the relatively coarse spatial distribution of ice-core sampling (red dots in Fig. 6), the SIPL thickness calculated by the VM model

30 at drill sites agrees well with the measurements (Fig. 6a), being graded "excellent" in contrast with the "poor" performance of the NVM model (Table 2). Despite efforts to tune the NVM model to give a better match with the observed SIPL

thickness, even a limited expansion of the SIPL can only be achieved with a considerable increase in the calculated T_{SC}^0 in disagreement with the observations.

For both VM and NVM models, the time series of area-averaged supercooling ($\overline{T_{SC}^0}$), FIC ($\overline{C_i}$), and SIPL thickness indicate

5   respectively two near-constant values and one near-constant growth rate after about the 150th day (Fig. 4b). This suggests some simple dependence of $\overline{T_{SC}^0}$ on frazil-ice-associated area-averaged SIPL thickening rate (ASTR) and $\overline{C_i}$ in the steady state. It is informative to explore how our various assumptions about the vertical distribution of FIC influence that relationship in the MMS region.

4.2 Dependence of SIPL thickening rate on ISW supercooling

10   The response of ice shelf basal melting (i.e. $T_{SC}^0 < 0$) to variations in ocean temperature has been investigated with observations (Rignot and Jacobs, 2002; Shepherd et al., 2004) and model results (Grosfeld and Sandhäger, 2004; Holland et al., 2008; Payne et al., 2007; Walker and Holland, 2007; Williams et al., 1998, 2002). In contrast, we know of no studies to date of the response of marine ice (or SIPL) thickening rate beneath ice shelves (or sea ice) to variations in supercooling (i.e. $T_{SC}^0 > 0$), which is of potential significance for evaluating the mass balance of deep-draughting ice shelves in cold water

15   environments and adjacent sea ice subject to climatic variability.

Owing to the number of poorly-constrained parameters in the frazil-ice-laden ISW plume model, we conducted 211 comparative sensitivity experiments between VM and NVM models, varying both physical and input parameters, including drag coefficient, frazil ice crystal size configuration, average number of frazil crystals, background current speed, width and

20   thickness of the ISW outflow, and FIC within the outflow (see Table 3). For all model runs, we plot the relationship between $\overline{T_{SC}^0}$ and ASTR in the steady state, using output from the last 30 days of each run (Fig. 7).

In Fig. 7a, the results of VM model are grouped by the prescribed supercooled layer thickness D_{SC}^{ini} in the ISW outflow. For the smaller $D_{SC}^{ini} < 65$ m, there is a relatively consistent increase in ASTR with increasing $\overline{T_{SC}^0}$, while for the larger $D_{SC}^{ini} \geq 65$

25   m, ASTR tends to be much more variable. It is worth mentioning that $D_{SC}^{ini} = 65$ m is exactly the value estimated by HU14 based on the measurements conducted by Lewis and Perkin (1985) and Jones and Hill (2001). For $D_{SC}^{ini} = 78$ m and greater, an inflexion point (stars in Fig. 7a) emerges separating a region of low ASTR, where ASTR tends to decrease with increasing $\overline{T_{SC}^0}$, from a region of high ASTR, where there is a very rapid increase in ASTR with increasing $\overline{T_{SC}^0}$. This complex response of the VM model must result from the consideration of vertical structure in the FIC, controlled by the frazil ice

30   suspension index Z_* (Fig. 2), in the calculation of frazil ice growth.

We therefore calculated the mean suspension index Z_*^a for all runs of VM and NVM models by

$$Z_*^a = w_{i,3}/\kappa\overline{u_*} = w_{i,3}/\kappa\sqrt{C_d}\,\overline{U}, \tag{4}$$

where subscript "3" denotes the intermediate frazil ice crystal size that tends to be the dominant component suspended in the ISW plume (Holland and Feltham, 2006; HU14; Smedsrud and Jenkins, 2004), the overbar denotes area-averaging. For each run, we grouped the results into 6 subranges of Z_*^a, and plotted separately both VM and NVM model results within each

5   subrange (Fig. 7b). For the VM model results, we find a monotonic increase in ASTR with increasing $\overline{T_{SC}^0}$ for each subrange of Z_*^a that can be fitted with an exponential function, and the calculated ASTR is discernibly larger than that calculated by the NVM model.

The maximum values of $\overline{T_{SC}^0}$ were obtained within the NVM model, because the supercooling is used more sufficiently to

10   produce SIPL in the corresponding runs in the VM than in the NVM model. However, we found variations within the VM model bands. With decreasing Z_*^a, the upper limit of $\overline{T_{SC}^0}$ for each band decreases first, and then increases. If Z_*^a is sufficiently large (band 1), the suspended frazil crystals deposit out of the ISW plume so rapidly that they cannot efficiently use the ISW supercooling to grow, leading to the smallest SIPL production for the VM model. For smaller Z_*^a (bands 2-4), the frazil crystals bathed in the supercooled layer of the ISW plume can remain in suspension and grow longer, resulting in a

15   thicker SIPL and less residual supercooling.

However, if Z_*^a decreases further (bands 5-6), higher FIC occurs within the lower overheated part of ISW plume, where melting of the crystals can mitigate the consumption of supercooling (Fig. 2b). That promotes further growth of frazil ice which can remain in suspension even longer, and thus lead to rapid SIPL production (band 6). These arguments can be

20   further illustrated by comparison of $\overline{T_{SC}^0}$ calculated by the VM and NVM models for all bands points (Fig. 8). In addition to the standard run, there are several runs in band 6 having larger $\overline{T_{SC}^0}$ values in the VM model. With increasing Z_*^a, the number of such runs decreases (band 5), and all runs have progressively larger $\overline{T_{SC}^0}$ in the NVM model from bands 4 to 1. Band 6 runs have the largest FIC within the lower overheated part of the ISW plume (as shown in Fig. 2b) where melting of frazil ice counteracts the consumption of supercooling by frazil growth in the upper part of the plume. As Z_*^a increases, the FIC within

25   the lower overheated part decreases, and finally vanishes, and the resulting release of supercooling in the upper part is more efficient in the VM model than in the NVM model. Accordingly, when Z_*^a becomes small enough, the two thermodynamic processes of efficient growth in the upper supercooled part of the plume and the maintenance of supercooling by melting of frazil in the lower part lead to the rapid growth of the SIPL.

30   In Fig. 7a, when $D_{SC}^{ini} < 65$ m, ISW supercooling is insufficient to distinguish runs with different Z_*^a. In other words, the relation between ASTR and $\overline{T_{SC}^0}$ is independent of Z_*^a. When D_{SC}^{ini} is within the range of 65 to 78 m, the VM model results are distinguishable, with data points having smaller ASTR and larger $\overline{T_{SC}^0}$ corresponding to larger Z_*^a (Fig. 7b). When $D_{SC}^{ini} \geq 78$

m, the inflexion points emerge, all of which correspond to data points within band 5 in Fig. 7b. That is, the ISW supercooling revives when Z_*^a less than the critical value between 2.1 and 2.5. Therefore, we conclude that when D_{SC}^{ini} exceeds a critical value (about 65 m for these MMS simulations), the efficiency of converting ISW supercooling into frazil ice growth is controlled by the suspension index.

5   ### 4.3 Dependence of FIC on ISW supercooling

In view of the correlation between SIPL thickening rate and FIC shown in Eq. (4) (also see Fig. 5e and f; Fig. 6b and c), we will explore the relationship between $\overline{T_{SC}^0}$ and $\overline{C_l}$ here. As expected, the complex response of $\overline{C_l}$ to variations in $\overline{T_{SC}^0}$ (Fig. 9) is similar to the relationship between $\overline{T_{SC}^0}$ and ASTR (Fig. 7) in the VM model. In Fig. 9a, there analogous inflexion points to those in Fig. 7a within band 5 (Fig. 9b) that emerge when $D_{SC}^{ini} \geq 78$ m, while we also find exponential growth of $\overline{C_l}$ with $\overline{T_{SC}^0}$

10   (Fig. 9b).

The magnitude of $\overline{C_l}$ calculated in the VM and NVM models is compared in Fig. 10a and b, where we find that the former are always larger than the latter. The differences increase with decreasing Z_*^a, probably because of the combined thermodynamic processes discussed above. We also note that the upper limit of $\overline{C_l}$ increases with decreasing Z_*^a, because the

15   frazil ice can remain in suspension and grow for longer before depositing out of the ISW plume. The large scatter of the points in band 6 is probably a reflection of the many sensitivity runs undertaken with varying parameters that had the drag coefficient and frazil size distribution set as they were for the standard run (see Table 3). The values of Z_*^a for all these points are similar to the value obtained in the standard run, and all lie within band 6. Nonetheless, the scatter exerts little influence on the general trend. Comparing the ASTR calculated with the VM versus the NVM model we see similar behavior, but with

20   greater differences between bands (Fig. 10c and d).

The exponential functions in Fig. 7b suggest possible relationships between ASTR and supercooling in MMS, but observations of suspended frazil ice crystal sizes and turbulence within the ISW would be needed to calculate Z_*^a. To date, there are limited observations of frazil ice in situ, and the majority of the observations that have been taken instruments not

25   specifically designed for ice crystal detection (Leonard et al., 2006).

5 Summary and conclusions

In this study, we demonstrated how the vertical profiles of supercooling and FIC within an ISW plume jointly determine the growth of suspended frazil ice, and thus the rate of SIPL formation. A new vertically-modified, frazil-ice-laden, ISW plume model which encapsulates these combined nonlinear effects was applied to the MMS region, and reproduced the observed

30   ISW supercooling and SIPL distributions in two horizontal dimensions. Using multiple model runs, the relationship between

ISW supercooling and SIPL thickening rate, as well as FIC, in MMS was explored: both SIPL thickening rate and FIC increase exponentially with ISW supercooling, with the complicated form of the relationship depending on the suspension index that controls the vertical distribution of FIC within the ISW plume. Moreover, when the thickness of a supercooled layer of ISW is large enough, the efficiency of converting ISW supercooling into FIC, and thus SIPL growth is determined
5   by the suspension index.

The exponential dependence of the SIPL thickening rate on ISW supercooling has the potential to provide insight into the formation of layers of marine ice beneath ice shelves, although further observations to constrain the relationship would be useful. To this end, observations in MMS, particularly focused in the western sound, near the ISW outflow region, where the
10   supercooled ISW plume and SIPL are prominent, would be particularly useful, as would observations that help to constrain the frazil size spectrum within the sea ice-ocean boundary layer. A simple relationship between supercooling and marine ice formation would be the key to parameterize the process in more three-dimensional, primitive equation ocean models which frequently neglect the ice-ocean boundary layer processes and the details of an evolving FIC distribution (Liu et al., 2017; Mueller et al., 2018; Stern et al., 2013). Further process studies, including the influence of vertical structure of current within
15   the ice shelf (or sea ice) -ocean boundary layer (Jenkins 2016) could also contribute. Finally, the performance of the VM model in providing reliable estimates of supercooling and frazil ice flux at the SIPL base makes it an attractive tool for coupling with sea ice models focused on microscale processes within the bottom layer of the ice (Buffo et al., 2018).

Data availability. The data archive associated with this study can be found in the Global Change Master Directory under the keyword K063_2011_2012_NZ_1.

20   *Author contributions.* CC led the study. The simulations were designed by ZW and CC, implemented by CL and RX, and analyzed by CC, AJ, and PRH. The paper was written by CC, AJ, and PRH.

Competing interests. Herby we declare that no competing interests is present for this study.

Acknowledgements. This work was funded by the National Natural Science Foundation of China (41406214, 41306208, 41606217). CC and CL were respectively supported by the China Scholarship Council (201708320046, 201504180026). ZW
25   was supported by "the Fundamental Research Funds for the Central Universities" (2017B04814, 2017B20714).

References

Arrigo, K. R., Mock, T., and Lizotte, M. P.: Primary producers and sea ice, Sea ice, 2, 283-325, 2010.

Bombosch, A. and Jenkins, A.: Modeling the formation and deposition of frazil ice beneath Filchner-Ronne Ice Shelf, J. Geophys. Res.-Oceans, 100, 6983-6992, http://dx.doi.org/10.1029/94JC03224, 1995.

Buffo, J. J., Schmidt, B. E., and Huber, C.: Multiphase Reactive Transport and Platelet Ice Accretion in the Sea Ice of McMurdo Sound, Antarctica, J. Geophys. Res.-Oceans, 123, 324-345, https://doi.org/10.1002/2017JC013345, 2018.

Cheng, C., Song, Z. Y., Wang, Y. G., and Zhang, J. S.: Parameterized expressions for an improved Rouse equation, Int. J. Sediment Res., 28, 523-534, http://dx.doi.org/10.1016/S1001-6279(14)60010-X, 2013.

5 Cheng, C., Huang, H., Liu, C., and Jiang, W.: Challenges to the representation of suspended sediment transfer using a depth-averaged flux, Earth Surf. Proc. Land, 41, 1337-1357, http://dx.doi.org/10.1002/esp.3903, 2016.

Cheng, C., Wang, Z., Liu, C., and Xia, R.: Vertical Modification on Depth-Integrated Ice Shelf Water Plume Modeling Based on an Equilibrium Vertical Profile of Suspended Frazil Ice Concentration, J. Phys. Oceanogr., 47, 2773-2792, http://dx.doi.org/10.1175/JPO-D-17-0092.1, 2017.

10 Dempsey, D. E., Langhorne, P. J., Robinson, N. J., Williams, M. J. M., Haskell, T. G., and Frew, R. D.: Observation and modeling of platelet ice fabric in McMurdo Sound, Antarctica, J. Geophys. Res.-Oceans, 115, https://doi.org/10.1029/2008JC005264, 2010.

Fricker, H. A., Popov, S., Allison, I., and Young, N.: Distribution of marine ice beneath the Amery Ice Shelf, Geophys. Res. Lett., 28, 2241-2244, https://doi.org/10.1029/2000GL012461, 2001.

15 Galton-Fenzi, B. K., Hunter, J. R., Coleman, R., Marsland, S. J., and Warner, R. C.: Modeling the basal melting and marine ice accretion of the Amery Ice Shelf, J. Geophys. Res.-Oceans, 117, http://dx.doi.org/10.1029/2012JC008214, 2012.

Gough, A. J., Mahoney, A. R., Langhorne, P. J., Williams, M. J., Robinson, N. J., and Haskell, T. G.: Signatures of supercooling: McMurdo Sound platelet ice, J. Glaciol., 58, 38-50, https://doi.org/10.3189/2012JoG10J218, 2012.

Grosfeld, K. and Sandhäger, H.: The evolution of a coupled ice shelf–ocean system under different climate states, Global
20   Planet. Change, 42, 107-132, http://dx.doi.org/10.1016/j.gloplacha.2003.11.004, 2004.

Holland, P. R. and Feltham, D. L.: The effects of rotation and ice shelf topography on frazil-laden ice shelf water plumes, J. Phys. Oceanogr., 36, 2312-2327, https://doi.org/10.1175/JPO2970.1, 2006.

Holland, P. R., Feltham, D. L., and Jenkins, A.: Ice shelf water plume flow beneath Filchner-Ronne Ice Shelf, Antarctica, J. Geophys. Res.-Oceans, 112, https://doi.org/10.1029/2006JC003915, 2007.

25 Holland, P. R., Jenkins, A., and Holland, D. M.: The response of ice shelf basal melting to variations in ocean temperature, J. Climate, 21, 2558-2572, https://doi.org/10.1175/2007JCLI1909.1, 2008.

Holland, P. R., Corr, H. F., Vaughan, D. G., Jenkins, A., and Skvarca, P.: Marine ice in Larsen ice shelf, Geophys. Res. Lett., 36, https://doi.org/10.1029/2009GL038162, 2009.

Hughes, K. G., Langhorne, P. J., Leonard, G. H., and Stevens, C. L.: Extension of an Ice Shelf Water plume model beneath
30   sea ice with application in McMurdo Sound, Antarctica, J. Geophys. Res.-Oceans, 119, 8662-8687, https://doi.org/10.1002/2013JC009411, 2014.

Hunkeler, P. A., Hoppmann, M., Hendricks, S., Kalscheuer, T., and Gerdes, R.: A glimpse beneath Antarctic sea ice: Platelet layer volume from multifrequency electromagnetic induction sounding, Geophys. Res. Lett., 43, 222-231, https://doi.org/10.1002/2015GL065074, 2016.

Jenkins, A.: A simple model of the ice shelf–ocean boundary layer and current, J. Phys. Oceanogr., 46, 1785-1803, http://dx.doi.org/10.1175/JPO-D-15-0194.1, 2016.

Jenkins, A. and Bombosch, A.: Modeling the effects of frazil ice crystals on the dynamics and thermodynamics of ice shelf water plumes, J. Geophys. Res.-Oceans, 100, 6967-6981, http://dx.doi.org/10.1029/94JC03227, 1995.

5   Jones, S. J. and Hill, B. T.: Structure of sea ice in McMurdo Sound, Antarctica, Ann. Glaciol., 33, 5-12, http://dx.doi.org/10.3189/172756401781818347, 2001.

Joughin, I. and Padman, L.: Melting and freezing beneath Filchner-Ronne Ice Shelf, Antarctica, Geophys. Res. Lett., 30, http://dx.doi.org/10.1029/2003GL016941, 2003.

Langhorne, P. J., Hughes, K. G., Gough, A. J., Smith, I. J., Williams, M. J. M., Robinson, N. J., Stevens, C. L., Rack, W.,
10   Price, D., Leonard, G. H., Mahoney, A. R., Haas, C., Haskell, T. G.: Observed platelet ice distributions in Antarctic sea ice: An index for ocean-ice shelf heat flux, Geophys. Res. Lett., 42, 5442-5451, https://doi.org/10.1002/2015GL064508, 2015.

Lewis, E. L. and Perkin, R. G.: The winter oceanography of McMurdo Sound, Antarctica, Oceanology of the Antarctic continental shelf, 145-165, https://doi.org/10.1029/AR043p0145, 1985.

15   Leonard, G. H., Purdie, C. R., Langhorne, P. J., Haskell, T. G., Williams, M. J. M., and Frew, R. D.: Observations of platelet ice growth and oceanographic conditions during the winter of 2003 in McMurdo Sound, Antarctica, J. Geophys. Res.-Oceans, 111, https://doi.org/10.1029/2005JC002952, 2006.

Liu, C., Wang, Z., Cheng, C., Xia, R., Li, B., and Xie, Z.: Modeling modified Circumpolar Deep Water intrusions onto the Prydz Bay continental shelf, East Antarctica, J. Geophys. Res.-Oceans, 122, 5198-5217,
20   http://dx.doi.org/10.1002/2016JC012336, 2017.

Luo, Z., Zhu, J., Wu, H., and Li, X.: Dynamics of the sediment plume over the Yangtze Bank in the Yellow and East China Seas, J. Geophys. Res.-Oceans, 122, 10073-10090, https://doi.org/10.1002/2017JC013215, 2017.

McCave, I. N. and Swift, S. A.: A physical model for the rate of deposition of fine-grained sediments in the deep sea, Geological Society of America Bulletin, 87, 541-546, https://doi.org/10.1130/0016-
25   7606(1976)87<541:APMFTR>2.0.CO;2, 1976.

Morgan, V. I.: Oxygen isotope evidence for bottom freezing on the Amery Ice Shelf, Nature, 238, 393, https://doi.org/10.1038/238393a0, 1972.

Mueller, R. D., Hattermann, T., Howard, S. L., and Padman, L.: Tidal influences on a future evolution of the Filchner–Ronne Ice Shelf cavity in the Weddell Sea, Antarctica, The Cryosphere, 12, 453, http://dx.doi.org/10.5194/tc-12-453-2018,
30   2018.

Oerter, H., Kipfstuhl, J., Determann, J., Miller, H., Wagenbach, D., Minikin, A., and Graft, W.: Evidence for basal marine ice in the Filchner–Ronne Ice Shelf, Nature, 358, 399, https://doi.org/10.1038/358399a0, 1992.

Padman, L. and Erofeeva, S.: Tide Model Driver (TMD) Manual, Version 1.2, Earth and Space Research, Seattle, Wash., 2005. [Available at www.esr.org/polar_tide_models/README_TMD.pdf, last accessed 7 Nov. 2012.]

Payne, A. J., Holland, P. R., Shepherd, A. P., Rutt, I. C., Jenkins, A., and Joughin, I.: Numerical modeling of ocean-ice interactions under Pine Island Bay's ice shelf, J. Geophys. Res.-Oceans, 112, http://dx.doi.org/10.1029/2006JC003733, 2007.

Price, D., Rack, W., Langhorne, P. J., Haas, C., Leonard, G., and Barnsdale, K.: The sub-ice platelet layer and its influence
5   on freeboard to thickness conversion of Antarctic sea ice, The Cryosphere, 8, 1031-1039, https://doi.org/10.5194/tc-8-1031-2014, 2014.

Ralston, D. K., Geyer, W. R., and Lerczak, J. A.: Structure, variability, and salt flux in a strongly forced salt wedge estuary, J. Geophys. Res.-Oceans, 115, C06005, https://doi.org/10.1029/2009JC005806, 2010.

Rees Jones, D. W. and Wells, A. J.: Frazil-ice growth rate and dynamics in mixed layers and sub-ice-shelf plumes, The
10   Cryosphere, 12, 25-38, http://dx.doi.org/ 10.5194/tc-12-25-2018, 2018.

Rignot, E. and Jacobs, S. S.: Rapid bottom melting widespread near Antarctic ice sheet grounding lines, Science, 296, 2020-2023, http://dx.doi.org/10.1126/science.1070942, 2002.

Rignot, E., Jacobs, S., Mouginot, J., and Scheuchl, B.: Ice-shelf melting around Antarctica, Science, 341, 266-270, https://doi.org/10.1126/science.1235798, 2013.

15   Robinson, N. J., Stevens, C. L., and McPhee, M. G.: Observations of amplified roughness from crystal accretion in the sub-ice ocean boundary layer, Geophys. Res. Lett., 44, 1814-1822, https://doi.org/10.1002/2016GL071491, 2017.

Robinson, N. J., Williams, M. J., Stevens, C. L., Langhorne, P. J., and Haskell, T. G.: Evolution of a supercooled Ice Shelf Water plume with an actively growing subice platelet matrix, J. Geophys. Res.-Oceans, 119, 3425-3446, https://doi.org/10.1002/2013JC009399, 2014.

20   Shepherd, A., Wingham, D., and Rignot, E.: Warm ocean is eroding West Antarctic ice sheet, Geophys. Res. Lett., 31, http://dx.doi.org/10.1029/2004GL021106, 2004.

Smedsrud, L. H. and Jenkins, A.: Frazil ice formation in an ice shelf water plume, J. Geophys. Res.-Oceans, 109, http://dx.doi.org/10.1029/2003JC001851, 2004.

Smith, I. J., Langhorne, P. J., Haskell, T. G., Trodahl, H. J., Frew, R., and Vennell, M. R.: Platelet ice and the land-fast sea
25   ice of McMurdo Sound, Antarctica, Ann. Glaciol., 33, 21-27, http://dx.doi.org/10.3189/172756401781818365, 2001.

Song, D. and Wang, X. H.: Suspended sediment transport in the Deepwater Navigation Channel, Yangtze River Estuary, China, in the dry season 2009: 2. Numerical simulations, J. Geophys. Res.-Oceans, 118, 5568-5590, http://dx.doi.org/10.1002/jgrc.20411, 2013.

Stern, A. A., Dinniman, M. S., Zagorodnov, V., Tyler, S. W., and Holland, D. M.: Intrusion of warm surface water beneath
30   the McMurdo Ice Shelf, Antarctica, J. Geophys. Res.-Oceans, 118, 7036-7048, https://doi.org/10.1002/2013JC008842, 2013.

Walker, R. T. and Holland, D. M.: A two-dimensional coupled model for ice shelf–ocean interaction, Ocean Model., 17, 123-139, http://dx.doi.org/10.1016/j.ocemod.2007.01.001, 2007.

Williams, M. J. M., Warner, R. C., and Budd, W. F.: The effects of ocean warming on melting and ocean circulation under the Amery Ice Shelf, East Antarctica, Ann. Glaciol., 27, 75-80, http://dx.doi.org/10.3189/1998AoG27-1-75-80, 1998.

Williams, M. J. M., Warner, R. C., and Budd, W. F.: Sensitivity of the Amery Ice Shelf, Antarctica, to changes in the climate of the Southern Ocean, J. Climate, 15, 2740-2757, http://dx.doi.org/10.1175/1520-0442(2002)015<2740:SOTAIS>2.0.CO;2, 2002.

Table 1: List of parameters used in standard model run.

Parameter	Value	Description
f	-1.4244×10^{-4} s^{-1}	Coriolis parameter
W_{ini}	3 km	ISW plume outflow width
$D_{ini}(D_{SC}^{ini})$	78 m	ISW plume outflow thickness (outflow supercooled layer thickness)
C_i^{ini}	1×10^{-6}	Depth-averaged volumetric FIC in outflow
N_{ice}	5	Number of frazil ice sizes
r_1, r_2, r_3, r_4, r_5	0.2, 0.6, 0.9, 1.2, 1.5 mm	Frazil ice radii for each class
a_r	0.02	Aspect ratio of frazil discs
$\bar{n}$	1×10^{3} m^{-3}	Average number of frazil crystals in all size classes per unit volume
C_d	0.02	SIPL basal drag coefficient
V_a	-0.01 m s^{-1}	Background flow speed
A_H	100 m^2 s^{-1}	Horizontal eddy viscosity
K_H	20 m^2 s^{-1}	Horizontal turbulent diffusivity
S_{ini}	34.59 psu	ISW plume outflow salinity
T_{ini}	$-0.0573 \times S_{ini} + 0.0832 + 7.61 \times 10^{-4}(z - D_{ini})$	ISW plume outflow temperature
θ_i	0.075	Shields criterion number

Table 2: List of calculated skill metrics for the results of VM and NVM standard model runs.

Varieties	RMSE		CC		SS	
	VM	NVM	VM	NVM	VM	NVM
T_{SC}^0	0.0070 °C	0.0069 °C	0.83	0.84	0.56	0.58
SIPL thickness	1.034 m	2.928 m	0.91	0.01	0.79	-0.65

Table 3: Parameter settings for sensitivity runs, indicated by check, colour-coded by ISW outflow thickness (bottom row). All other parameters remain as they were for the standard model run.

		Drag coefficient				
		0.015	0.0175	0.02	0.0225	0.025
	A: (0.2,0.6,0.9,1.2,1.5)	✓✓✓✓✓✓✓		✓✓✓✓✓✓		✓✓✓✓✓✓
	1.125×A		✓✓✓✓✓✓		✓✓✓✓✓✓	
	1.25×A		✓✓✓✓✓✓		✓✓✓✓✓✓	
Frazil size configuration (mm)	1.375×A		✓✓✓✓✓✓		✓✓✓✓✓✓	
	1.5×A	✓✓✓✓✓✓✓		✓✓✓✓✓✓✓		✓✓✓✓✓✓
	1.625×A		✓✓✓✓✓✓		✓✓✓✓✓✓	
	1.75×A		✓✓✓✓✓✓		✓✓✓✓✓✓	
	1.875×A		✓✓✓✓✓✓		✓✓✓✓✓✓	
	2×A	✓✓✓✓✓✓✓		✓✓✓✓✓✓✓		✓✓✓✓✓✓
W_{ini}	1 km			✓✓✓✓✓✓		
	5 km			✓✓✓✓✓✓		
C_i^{ini}	0.2×10⁻⁶			✓✓✓✓✓✓		
	5×10⁻⁶			✓✓✓✓✓✓		
V_a	0			✓✓✓✓✓✓		
	-0.02 m s⁻¹			✓✓✓✓✓✓		
$\bar{n}$	200 m⁻³			✓✓✓✓✓✓		
	5000 m⁻³			✓✓✓✓✓✓		
$D_{ini}(D_{SC}^{ini})(m)$		✓ ✓	✓	✓	✓	✓ ✓ ✓
		30 50	65	70	78	95 100 110
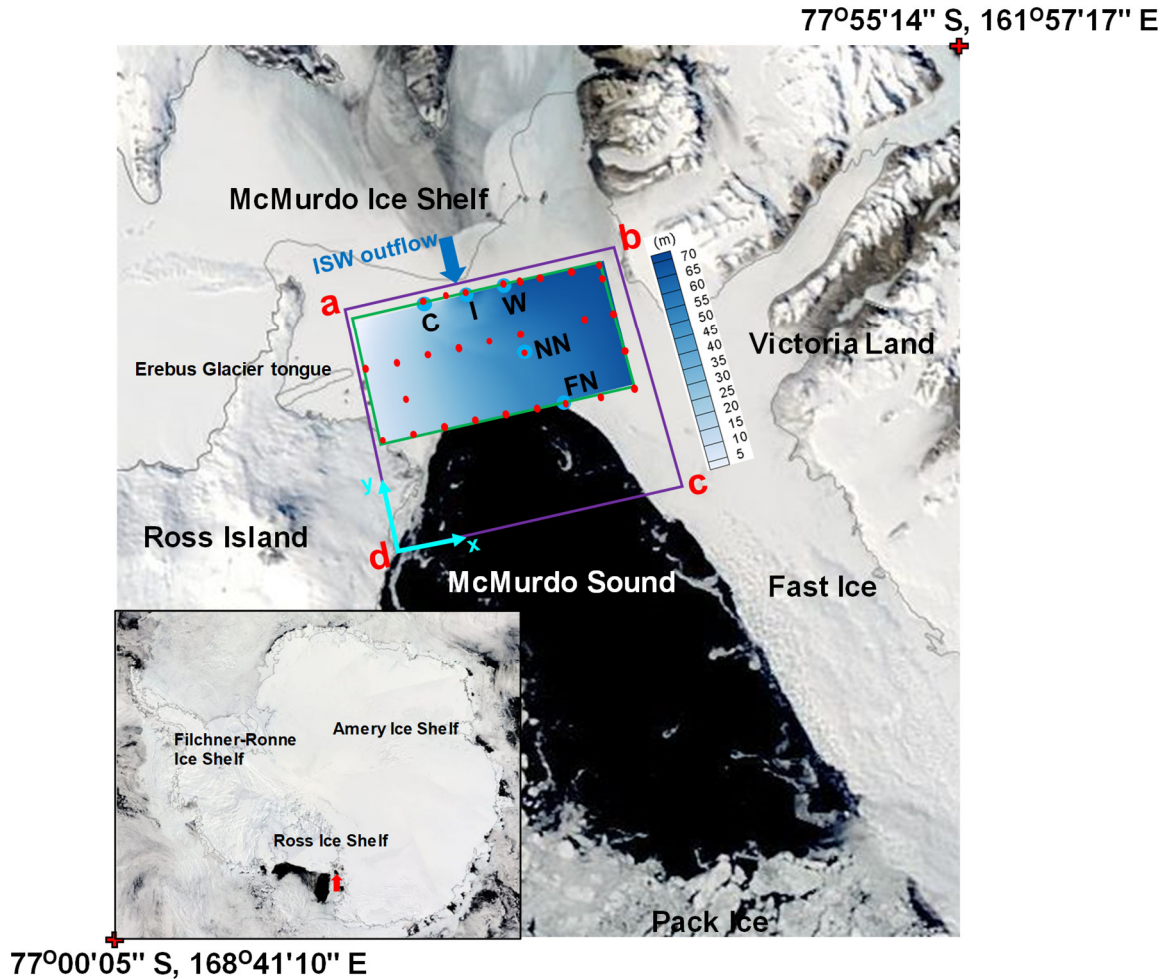
Figure 1: Satellite image of MMS region on 29 Nov. 2011. Purple and green frames outline the model and ice borehole (Fig. 6) domains, respectively. Colours within the green frame indicate the steady state ISW plume thickness calculated by the vertically-modified ISW plume model in the standard run (Fig. 5b). Light gray lines outline McMurdo Ice Shelf front and coastlines. Model boundaries d-a, a-b (except the ISW outflow) and "b-c" are treated as solid walls, while "c-d" is an open boundary. Blue and red dots respectively mark the oceanographic CTD and ice drilling sites, and the blue arrow represents the location of the ISW outflow in the model. Oceanographic and SIPL data are from measurements taken between late November and early December in 2011 (HU14). The red arrow in the inset (bottom-left) points to the location of the MMS region. Satellite image: NASA Rapid Response MODIS Subsets (http://earthdata.nasa.gov/data/near-real-time-data/rapidresponse/modis-subsets).
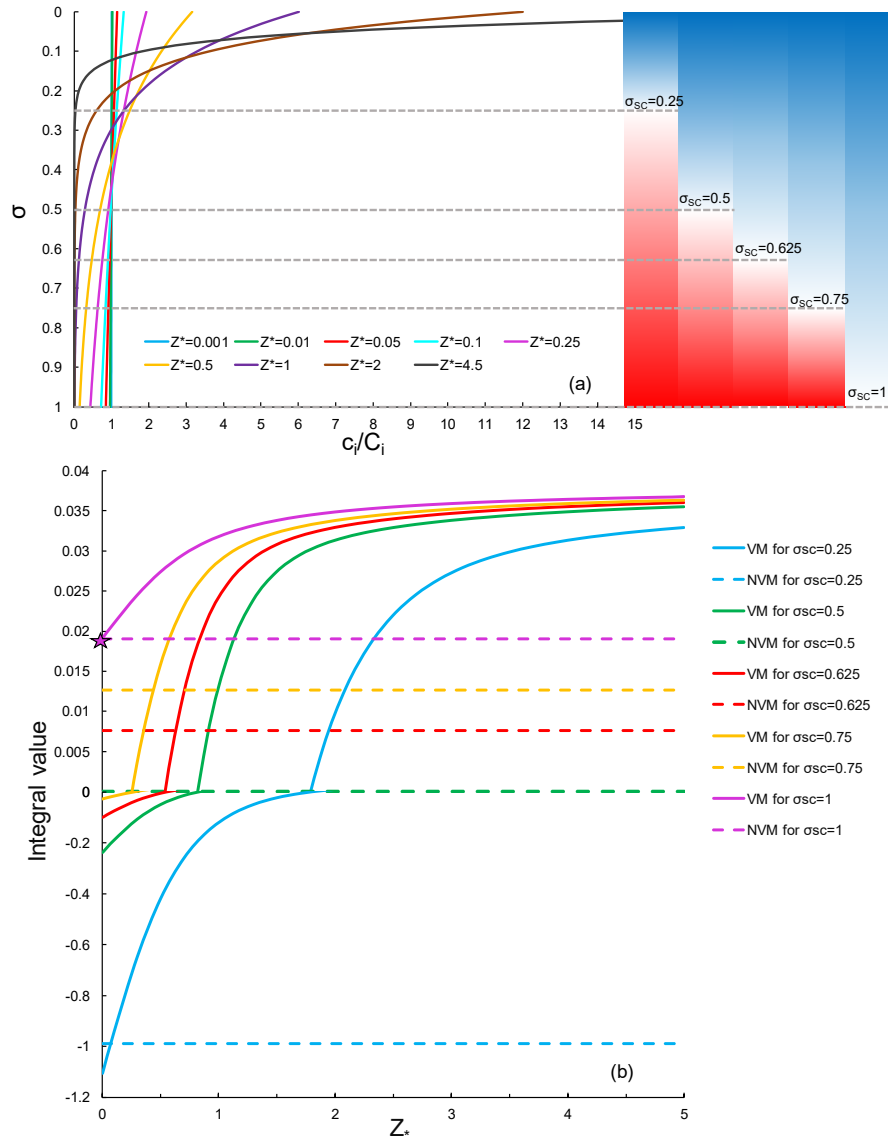
Figure 2: (a) Exponential profiles of equilibrium FIC for selected values of Z_*. Coloured bars at the right and horizontal dashed lines indicate the distribution of supercooling (blue, $T_{SC} > 0$) and overheating (red, $T_{SC} < 0$) for the values of σ_{SC} used in (b). **(b)** Dependence of integral value of I_{gr} on Z_* for suspended frazil ice freezing ($I_{gr} > 0$) and melting ($I_{gr} < 0$) under the supercooling conditions shown in (a). The star denotes the particular conditions under which the integral values of I_{gr} calculated using NVM and VM formulations are equal. Note that different y-axis scales are used for freezing and melting.
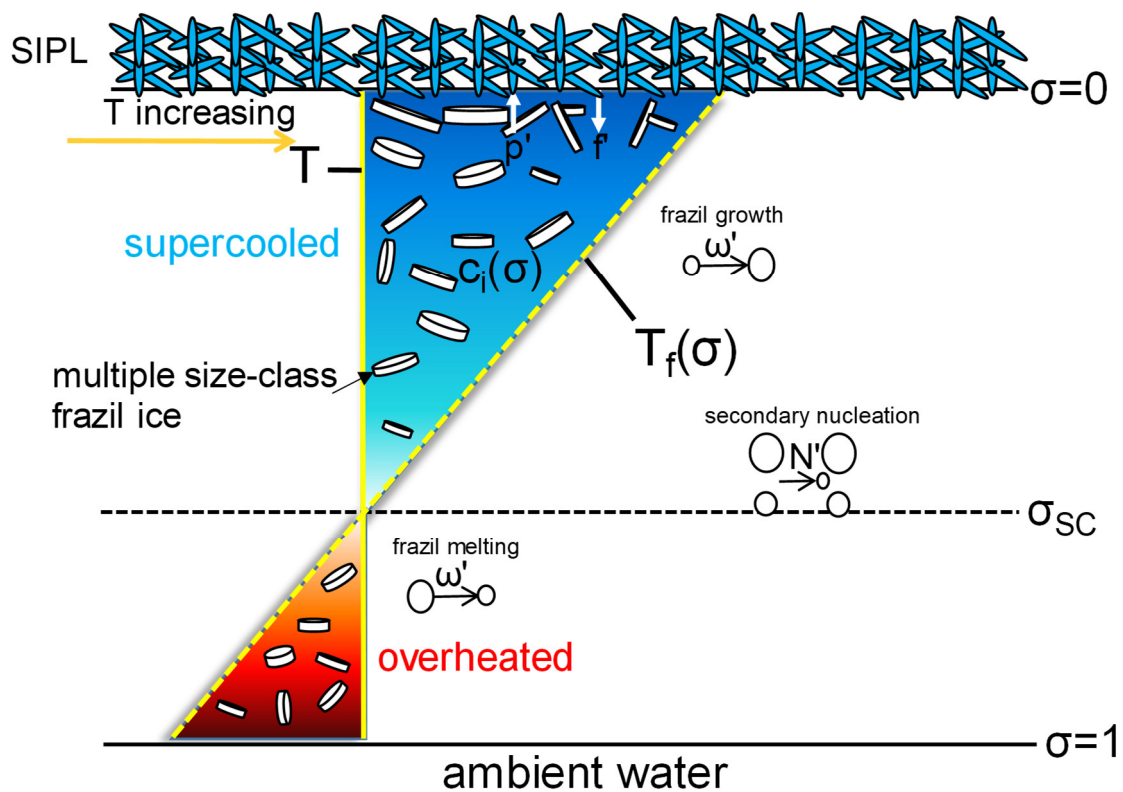
Figure 3: Schematic diagram of vertical distribution of thermal forcing and relevant processes within a supercooled ISW plume. The secondary nucleation is the process in which the frazil ice in the smallest class is supplemented by the collisions between other larger frazil ice crystals.
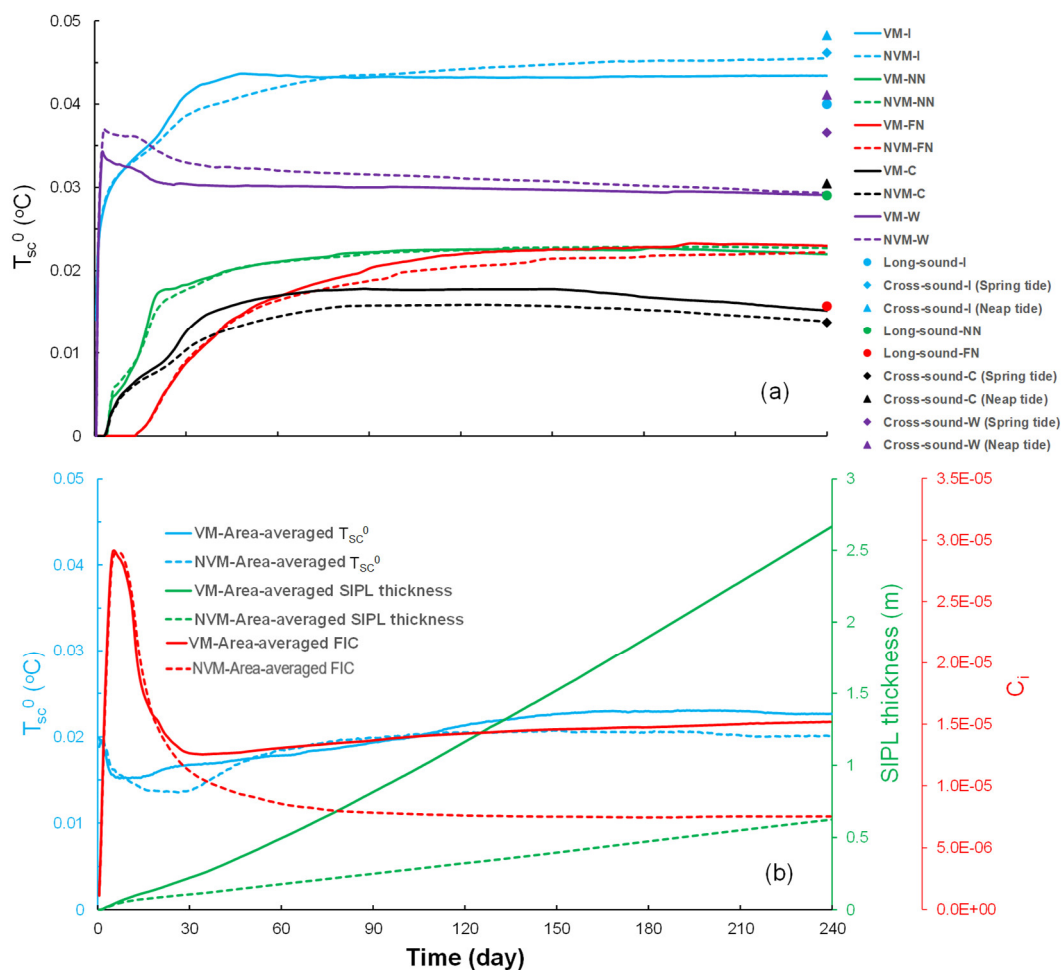
Figure 4: (a) Time series of T_{SC}^0 simulated by VM (solid lines) and NVM (dashed lines) models at five oceanographic sites (colour-coded) in the MMS region. (b) Time series of area-averaged T_{SC}^0 (blue), SIPL thickness (green), and FIC (red) simulated by VM (solid lines) and NVM (dashed lines) models over the model domain (purple frame in Fig. 1).
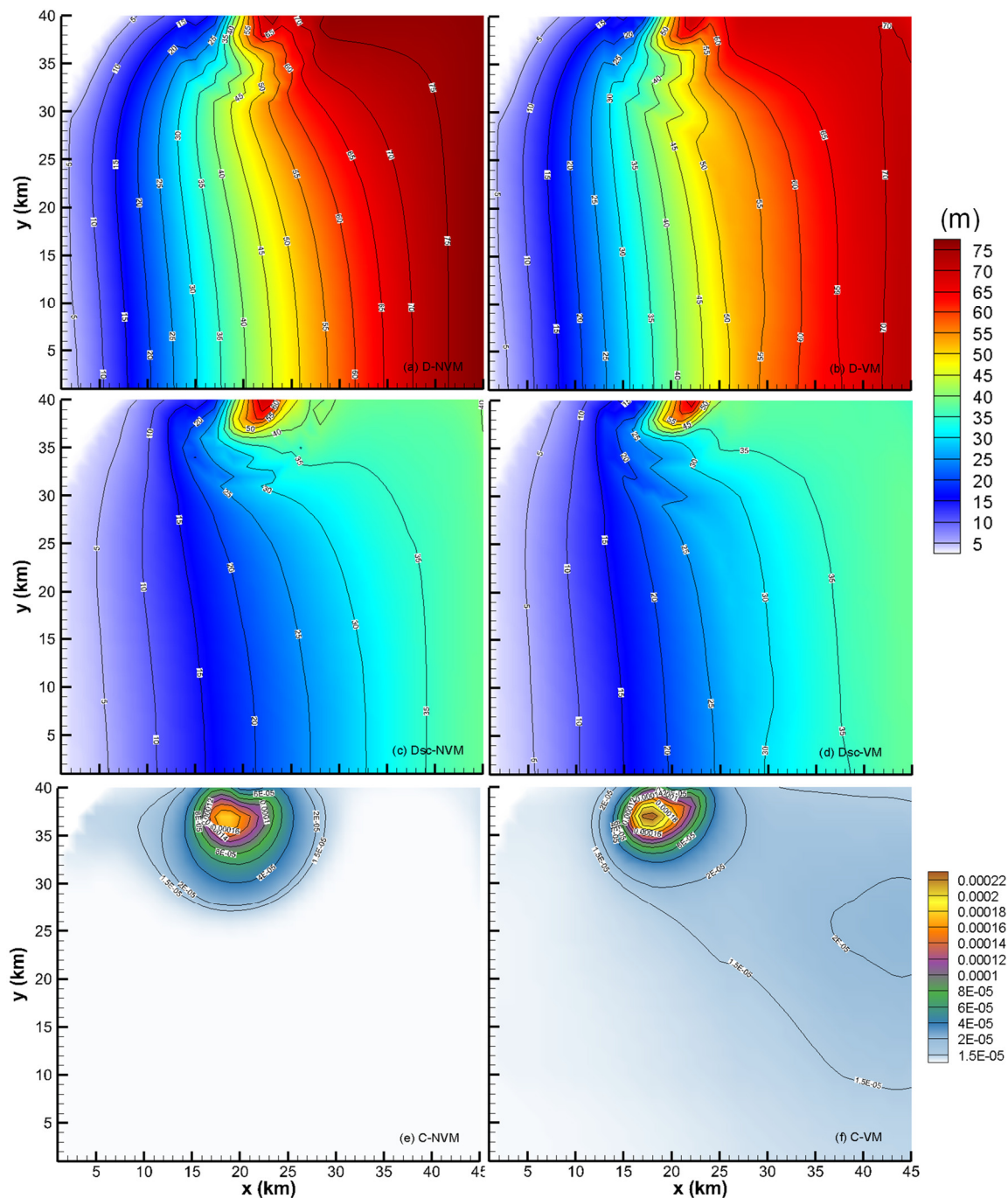
Figure 5: Spatial patterns of (a), (b) total, (c), (d) supercooled ISW plume thickness, and (e), (f) depth-averaged FIC at the end of the standard runs of (a), (c), (e) NVM and (b), (d), (f) VM over the model domain (purple frame in Fig. 1). Note that the colour scale used in (a-d) is unified.
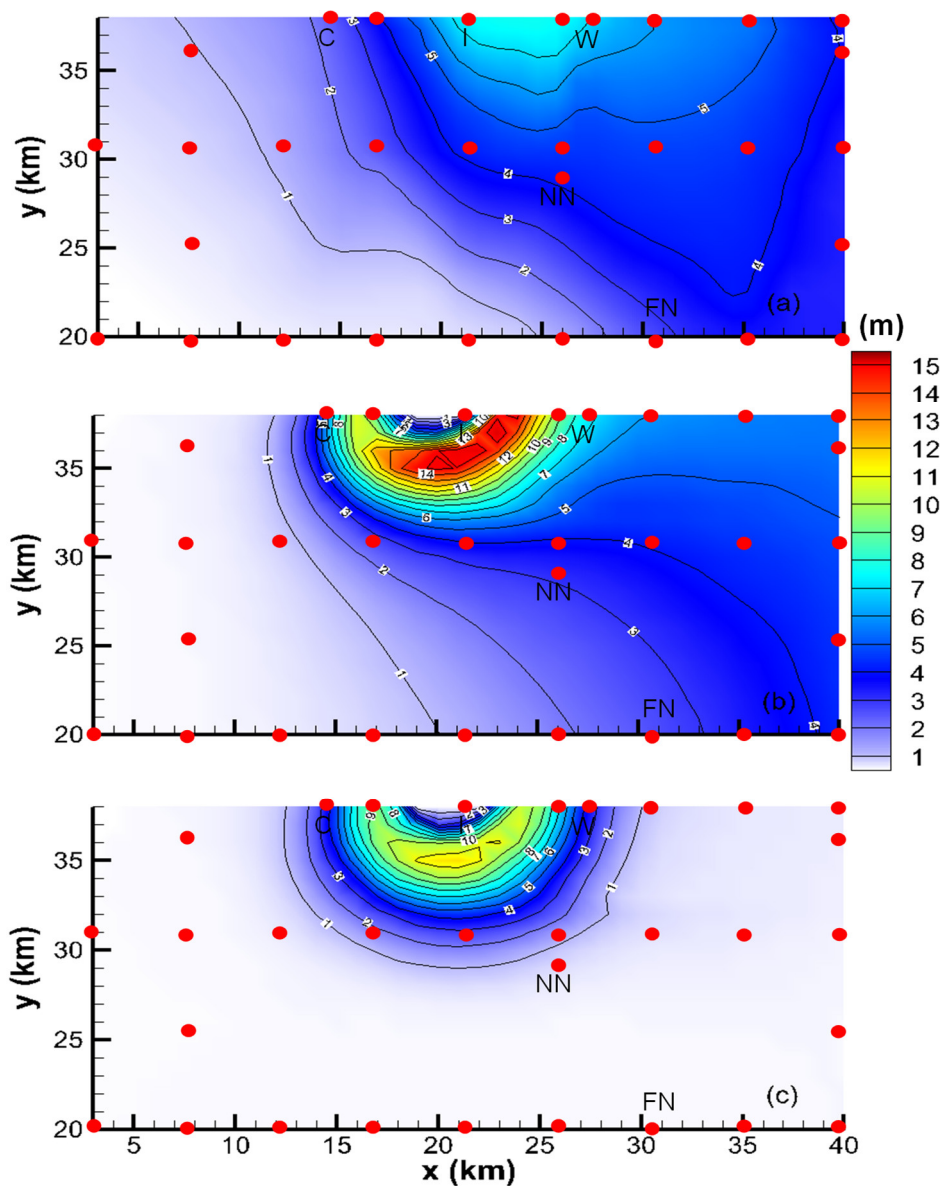
Figure 6: (a) SIPL thickness over green box in Fig. 1 interpolated from ice-core measurements (red dots). (b) and (c) SIPL thickness derived from (b) VM and (c) NVM models. Note that the colour scale is unified.
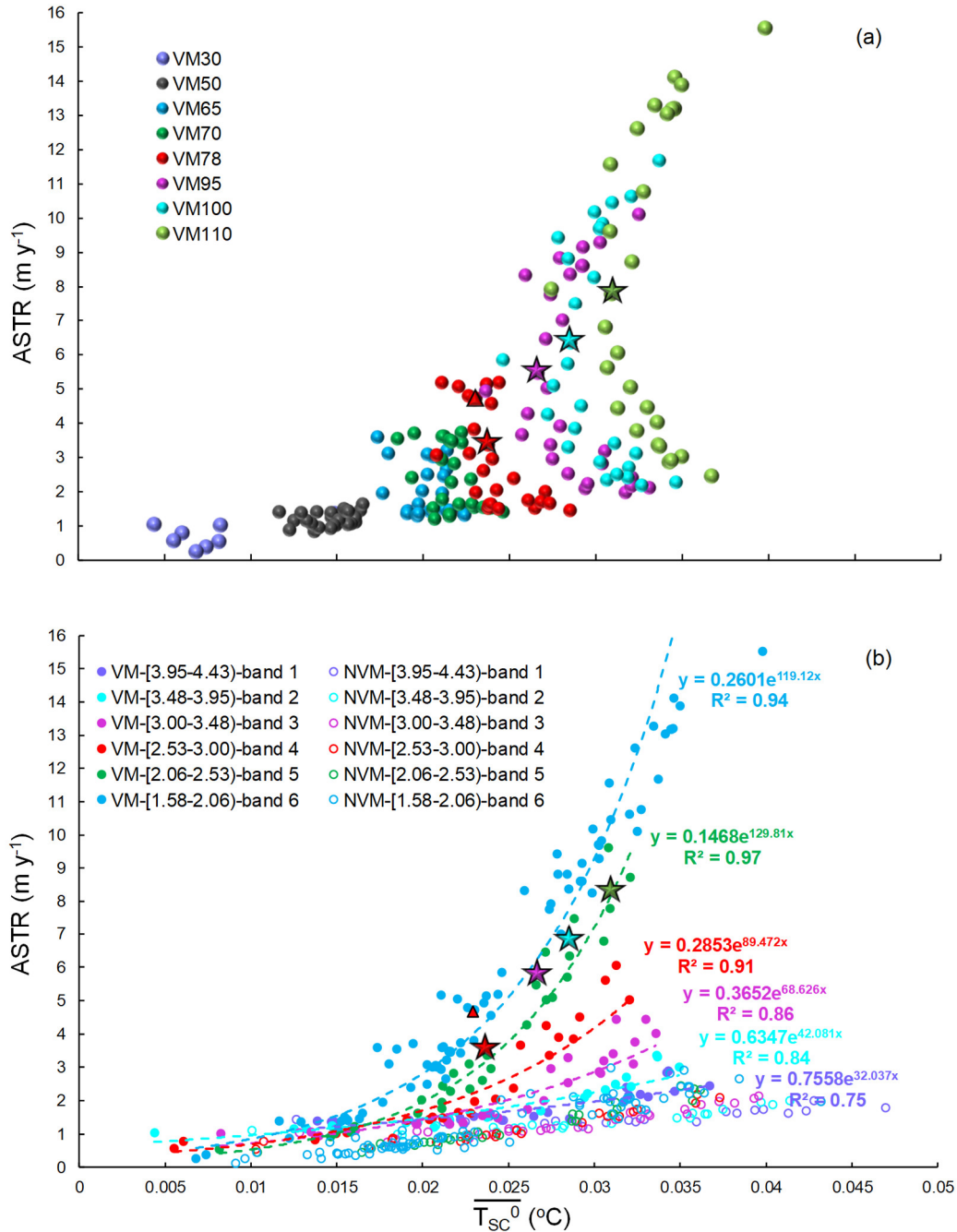
Figure 7: Relationship between $\overline{T_{SC}^0}$ and ASTR classified by (a) outflow supercooled layer thickness D_{SC}^{ini} and (b) mean frazil ice suspension index Z_*^a. Stars denote inflexion points for the runs with $D_{SC}^{ini} \geq 78$ m. Least squares fits to the data groups in (b) are indicated by dashed lines with corresponding equations. Numbers in legends of (a) and (b) represent the values of D_{SC}^{ini} and Z_*^a, respectively. Triangles correspond to the standard run.
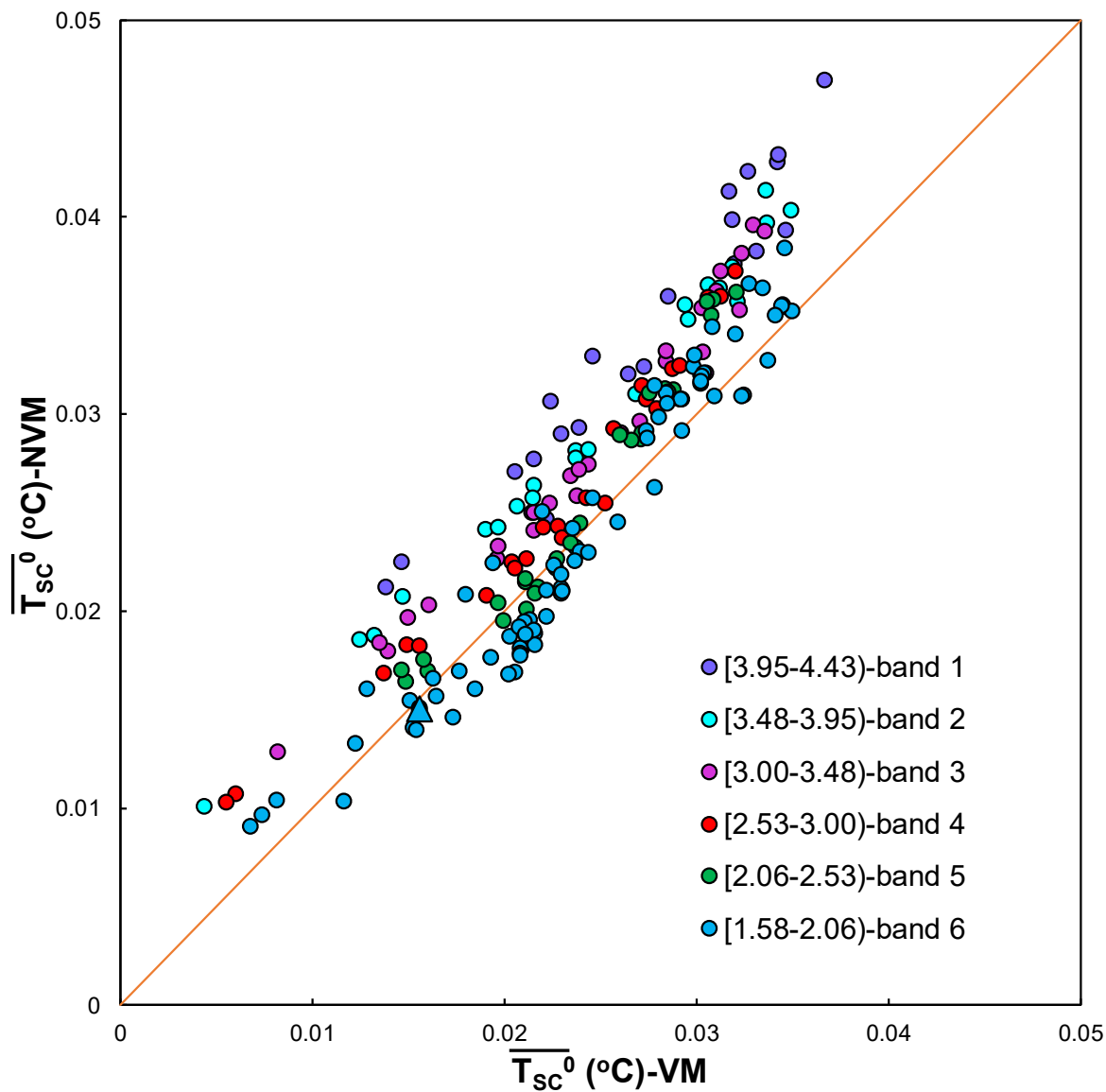
Figure 8: Comparison of $\overline{T_{SC}^0}$ calculated by the VM and NVM models for all sensitivity runs. Triangle corresponds to the standard run.
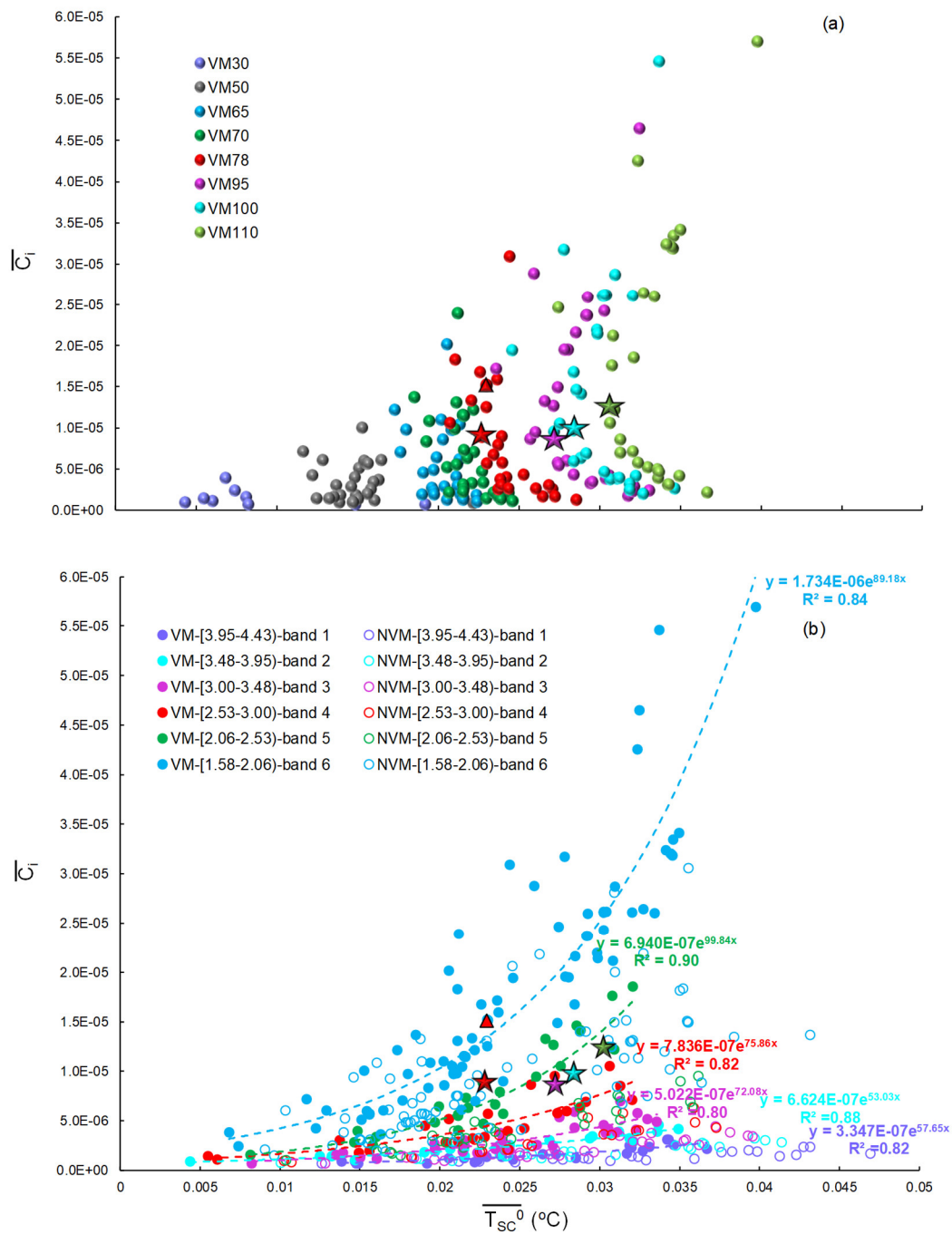
Figure 9: Same as Fig. 7, but for the relationship between $\overline{T^0_{SC}}$ and $\overline{C_\iota}$.
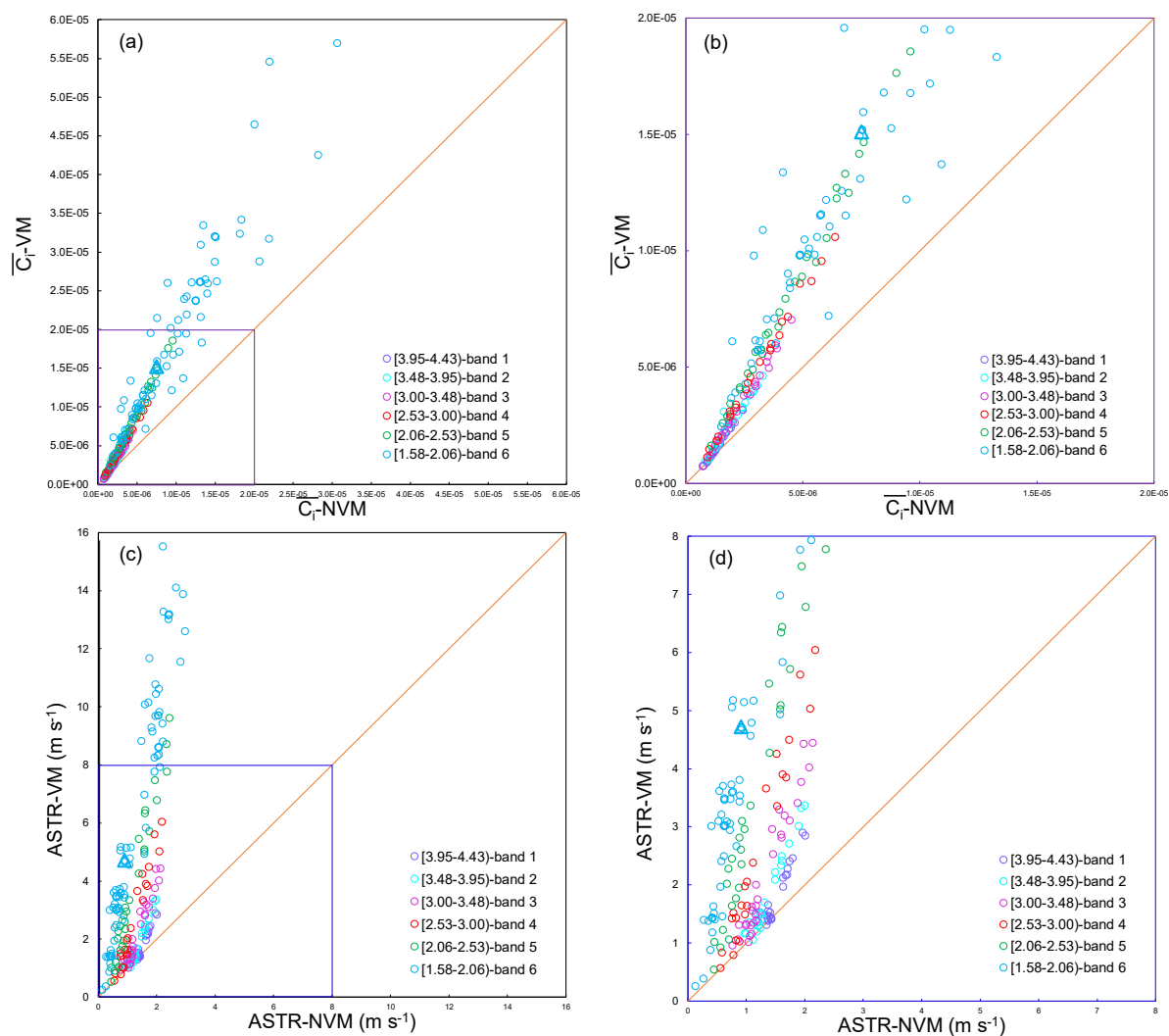
Figure 10: Comparison of (a), (b) $\overline{C}_i$ and (c), (d) ASTR calculated by the VM and NVM models for all sensitivity runs. Triangles correspond to the standard run. Enlargements of (b) $\overline{C}_i$ and (d) ASTR correspond respectively to the purple and blue frames in (a) and (c).